

Tracing the Effects of Calcium, Stannum, and Zinc Additions on the Creep Resistance of Mg–Al-Based Alloys



TAO CHEN, QINGHUAN HUO, SIJIA HU, CHUNYU WANG, YUXIU ZHANG, ZHIROU ZHANG, SHIQI LI, and XUYUE YANG

In this work, the effects of Ca, Sn, and Zn additions on the creep resistance of Mg–Al-based alloys were systematically traced at 453 K. The best creep resistance was obtained in Mg–6Al–1Ca (AX61) alloy followed by Mg–6Al–1Zn (AZ61) and Mg–6Al–1Sn (AT61) alloys, albeit the highest yield stress was obtained in AZ61 alloy at both room temperature and creep temperature. Specifically, for AT61 alloy, unsharp solution strengthening, ineffective precipitation strengthening, and long slip traces derived from prismatic $\langle a \rangle$ dislocations were responsible for the fastest creep rate and the most diminished creep resistance. For AZ61 alloy, the highest fraction of dynamic precipitates was achieved, creating the most serious depletion of solution strengthening. But due to the close connection between precipitates and dislocations, the effective precipitation strengthening avoided the weak creep resistance like the case in AT61 alloy. For AX61 alloy, strong solution strengthening and stable dislocation networks composed by prismatic $\langle a \rangle$ dislocations simultaneously reduced the creep rate. The limited loss of solution strengthening and the interrupted basal slip transitivity between neighboring grains also enhanced the creep resistance. Thus, it is strongly recommended that adding Ca element into Mg–Al-based alloys has a positive effect on the creep resistance *via* controlling solution strengthening and dislocation morphologies.

<https://doi.org/10.1007/s11661-023-07050-8>

© The Minerals, Metals & Materials Society and ASM International 2023

I. INTRODUCTION

Mg–Al–based alloys, due to low density and outstanding mechanical properties, have become the most common series and achieved ample attention in various domains, such as automobile and communication.^[1–3] However, it is worth noting that Mg–Al-based alloys are difficult to safely work at elevated temperatures. One of the predominant obstacles is the dramatic loss of strength in the high-temperature environment. The successive coarsening of Mg₁₇Al₁₂ phases, particularly dynamic precipitated ones, is responsible for the weak creep resistance.^[4–6] Specifically, researches concerning precipitation behaviors have shown that the precipitates with the habit plane parallel to the *c*-axis have a long-time valid precipitation strengthening effect

on the creep resistance.^[7] Such precipitation behavior and enhanced creep resistance have been found in Mg alloys with rare-earth (RE) addition.^[8–10] But unfortunately, abundant studies have indicated that the habit plane of Mg₁₇Al₁₂ precipitates in Mg–Al-based alloys are perpendicular to the *c*-axis and scarcely have any other precipitate variant with its habit plane parallel to the *c*-axis. Consequently, Mg–Al-based alloys are still hard to serve as the creep-resistant Mg alloys.^[11,12]

Apart from dynamic precipitation, static precipitation derived from aging treatment was once considered as a valid method for enhancing the creep resistance of Mg–Al-based alloys, but recent studies have demonstrated that the age-hardening response is not conspicuous in AZ series alloys.^[4,13,14] The addition of alloying elements is deemed to be the other simple and feasible strategy, such as RE elements.^[9,15,16] But in view of the high price of RE elements, RE-free elements for Mg–Al-based alloys have become the current mainstream to improve the heat-resistant properties like the case in the mechanical properties at room temperature.^[17,18] Calcium (Ca), as a promising alloying element owing to its low cost and density, exhibits outstanding characteristics. For instance, solution strengthening triggered by increasing Ca addition lower than 2 wt

TAO CHEN, QINGHUAN HUO, SIJIA HU, CHUNYU WANG, YUXIU ZHANG, ZHIROU ZHANG, SHIQI LI, and XUYUE YANG are with the School of Materials Science and Engineering, Central South University, Changsha 410083, P.R. China. Contact e-mail: huoqinghuan@csu.edu.cn

Manuscript submitted February 2, 2023; accepted March 31, 2023.

Article published online April 21, 2023

pct can sharply increase the yield stress.^[19] Another advantage is slightly weakening basal texture, leading to the weakened mechanical anisotropy and an excellent combination of multidirectional performance.^[20,21] Stannum (Sn), due to the high solid solubility in Mg matrix, strongly implies that Sn-containing Mg alloys would have an excellent age-hardening response. For example, some studies have confirmed the improved heat resistance of Mg–Zn alloys *via* adding Sn element.^[22,23] In addition, the formation of intermetallic compounds or fine precipitates, with high melting point and superior thermal stability, are expected to be an extra factor for enhance creep properties, such as the Ca-rich compounds in Mg–Ca-based alloys and the fine Mg₂Sn precipitates in Mg–Sn-based alloys.^[24–27]

For a long time, previous studies have focused on the effect of grain size, texture, and precipitate type on the mechanical properties of Mg–Al-based alloys *via* adding Ca or Sn elements.^[21,28–31] Recently, some studies began to unveil the effect of Ca and Sn alloying on the creep properties of cast Mg–Al-based alloys. Zhu *et al.*^[32] investigated the creep behaviors of squeeze-cast Mg–9Al–1Ca alloy. The alloy exhibited strong creep resistance with the assistance of the eutectic Ca-rich compounds. Kim *et al.*^[33] studied the creep behaviors of Mg–4Al–2Sn and AZ91 alloys at 423 K and 473 K. The better creep resistance was found in the former alloy at both temperatures. It was deduced that the widespread Mg₂Sn precipitates were able to impede grain boundary migration. Based on the above-mentioned reports, alloying Ca and Sn elements have been confirmed to have a positive effect on the creep resistance due to the formation of Ca-rich compounds and Mg₂Sn precipitates. But note that these results have all ignored the role of Mg₁₇Al₁₂ phases during creep process. Since the Mg₁₇Al₁₂ phase is the most common precipitate in the Mg–Al-based alloys, it is of much importance to know the effect on the dynamic precipitation of Mg₁₇Al₁₂ phase and the resultant creep properties after alloying different third elements.

In this work, Ca and Sn elements are selected to study the corresponding effects on the creep properties of Mg–Al-based alloys. The commercial AZ61 alloy is treated as a comparable one, due to its good combination of rolling ability during sample preparation and dynamic precipitation response during creep loading.^[1,4] For the sake of adding the same content with zinc (Zn) in AZ61 alloy, 1 wt pct Ca and 1 wt pct Sn elements are added, respectively. Since the solubility of Ca in Mg matrix is ~ 1.3 wt pct,^[34] the Ca content in this work can successfully avoid any effect on the main role of Mg₁₇Al₁₂ phase in Mg–6Al–1Ca (AX61) alloy. The solubility of Sn in Mg matrix is over 10 wt pct,^[35] so the main role of Mg₁₇Al₁₂ phase will certainly not be robbed in Mg–6Al–1Sn (AT61) alloy. With the designed compositions, this work aims to complement the understanding on the creep behaviors of Mg–Al-based alloys and provide a novel orientation for designing creep-resistant Mg alloys with low cost.

II. EXPERIMENTAL PROCEDURES

High-purity Mg (99.99 wt pct), pure Al (99.99 wt pct), and two master alloys, with nominal compositions of Mg–30 wt pct Ca and Mg–20 wt pct Sn, were employed in this work. These raw materials were molten *via* casting in an electric resistance furnace at 963 K under a protective atmosphere of CO₂ and SF₆ in a ratio of 100:1. Two ingots, AX61 and AT61 (wt pct), were prepared after casting, respectively. As a comparison, a commercial AZ61 cast alloy was also used in this work. The chemical compositions are listed in Table 1. The three ingots were homogenized at 703 K for a dwell time of 24 hours, then all immediately followed by air cooling. The same total reduction of ~ 50 pct were carried out using hot rolling at 703 K. In order to acquire twin-free and equiaxed microstructure, AX61 alloy was subjected to solid solution treatment at 623 K for 6 hours, AT61 alloy was solution treated at 653 K for 2 hours, and AZ61 alloy was solution treated at 693 K for 6 hours, then all alloys were quenched in water. The directions for the hot-rolled plates were thereafter labeled as the RD (rolling direction), ND (normal direction), and TD (transverse direction).

Samples with a gauge length of 9 mm along the RD and a cross section of 3 × 1 mm² for uniaxial tensile tests and tensile creep tests were machined. Tensile properties at room temperature and 453 K were measured along the RD on an Instron-type mechanical testing machine at a strain rate of 3 × 10⁻³ s⁻¹. Tensile creep tests were performed along the RD at an operating temperature of 453 K under a wide window of stress ranging from 60 to 90 MPa. Remarkably, samples were pre-heated at 453 K for 10 minutes before loading, and immediately quenched into water after creep tests.

The microstructures and crystallographic orientations were obtained *via* optical microscopy (OM) and scanning electron microscopy (SEM) equipped with an electron backscatter diffraction (EBSD) apparatus before and after creep tests. Transmission electron microscopy (TEM) and high-angle annular dark-field (HAADF) analysis were used to observe precipitates and dislocations under the two-beam mode after creep tests. For OM observations, samples were mechanical polishing, and etched in acetic picral (4 g picric acid, 10 ml water, 10 ml acetic, and 70 ml ethanol). For SEM and EBSD observations, samples were prepared by mechanical polishing, and electropolishing in a 1:9 volume ratio of HNO₃ and C₂H₅OH mixed solution. For TEM samples, disks were cut with a diameter of 3 mm, which were mechanically grounded to 80 μm and subsequently perforated *via* ion milling.

III. RESULTS

A. Initial Microstructures

The initial microstructures are created after solid solution treatments, as shown in the OM images and inverse pole figures (IPFs) in Figure 1. The microstructures obtained in these samples are all characterized by

Table I. Chemical Compositions of AX61, AT61, and AZ61 Alloys in this Work (in Weight Percent)

Alloy	Al	Ca	Sn	Zn	Mn	Cu	Fe	Si	Mg
AX61	6.02	0.98	—	—	—	—	—	—	bal
AT61	6.08	—	1.33	—	—	—	—	—	bal
AZ61	5.96	—	—	0.86	0.22	0.012	0.005	0.008	bal

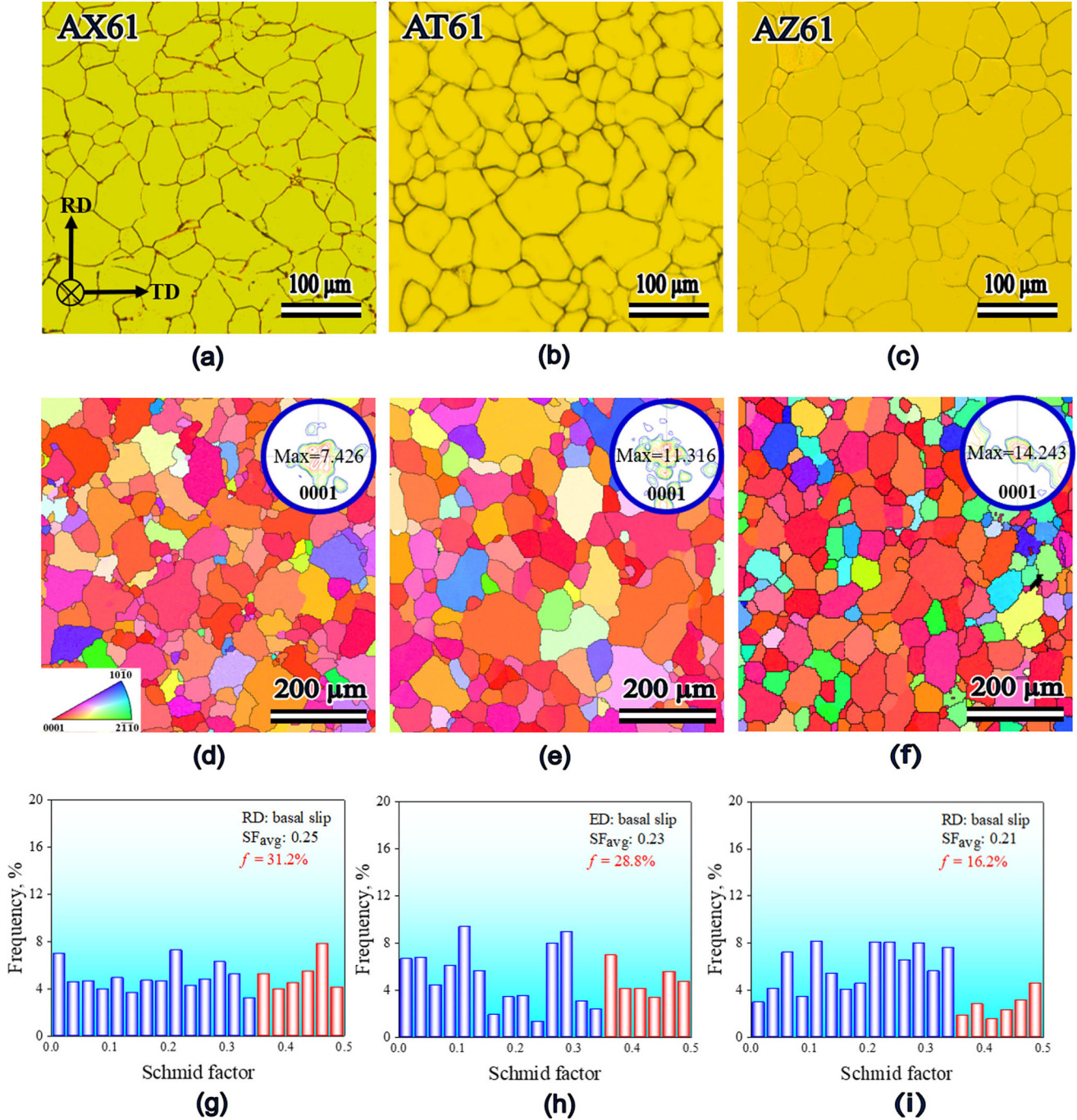


Fig. 1—(a) through (c) Typical OM images, (d) through (f) inverse pole figures (IPFs), and (g) through (i) Schmid factor distribution for basal slip along the RD in AX61, AT61, and AZ61 alloys before creep tests.

twin-free and equiaxed grains. The average grain size for AX61 sample is $\sim 68 \mu\text{m}$, while $\sim 78 \mu\text{m}$ in size is obtained for AT61 sample and $\sim 73 \mu\text{m}$ for AZ61 sample *via* a linear intercept method. The investigated samples have a similar rolling texture, wherein most of the basal poles are aligned parallel to the ND. The texture intensity is 7.426 for AX61 sample, then increases to 11.316 and 14.243 for AT61 and AZ61 samples, respectively. Figures 1(g) through (i) show the Schmid factor distributions for basal slip in all samples. Although the average Schmid factor value is similar, the fraction above 0.35 is much higher in AX61 and AT61 samples compared to AZ61 sample. Causing such differences are probably attributed to adding different atoms into Mg–Al-based alloys, which has been considered to be pertinent to the texture weakening *via* alloying Ca element and the opposite results *via* alloying Zn element.^[36]

B. Uniaxial Tensile Properties

Figures 2(a) and (b) show typical engineering stress–strain curves of all the samples at 298 K and 453 K. The corresponding yield stresses of all samples are measured along the RD at both room temperature and creep temperature, as shown in Figure 2(c). It is seen that AZ61 sample has the highest yield stress at both two temperatures, which are consistent with the low Schmid factors for basal slip and the texture hardening effect.^[37] Table II summarizes the yield stress values of all samples with error ranges. Their yield stresses are 155, 168, and 198 MPa for AX61, AT61, and AZ61 samples at room temperature. At 453 K, the yield stresses decrease to 132, 127, and 151 MPa, respectively.

C. Tensile Creep Behaviors

Figure 3 presents the creep strain *vs.* creep time curves of AX61, AT61, and AZ61 samples crept along the RD at 453 K under an applied stress range of 60 to 90 MPa. The creep strain continuously increases with the increasing creep time, as clearly revealed in Figure 3. A remarkable acceleration in creep strain is observed in AT61 sample, followed by AZ61 and AX61 samples,

indicating that the creep resistance of AX61 sample is the strongest. Correspondingly, Table III summarizes the steady creep rate of AX61, AT61, and AZ61 samples measured from their steady creep stages. Interestingly, being different from the increasing yield stress from AX61 to AZ61 samples, the creep resistance in the three samples does not show the synchronous improvement order. Although AZ61 sample shows the highest yield stress at both room temperature and creep temperature, it does not own the best creep resistance. Instead, AX61 sample exhibits the strongest creep resistance, followed by AZ61 and AT61 samples. The unexpected changes in the creep resistance will be analyzed in the discussion section.

Admittedly, the steady creep rate strongly depends on the applied stress level and the creep temperature. The creep mechanisms can be empirically reflected *via* the stress exponent (n), which is usually described by modifying the power law equation^[38]:

$$n = \left(\frac{\partial \ln \dot{\epsilon}}{\partial \ln \sigma} \right)_T \quad [1]$$

Here, σ stands for the applied stress, T represents the absolute temperature, and $\dot{\epsilon}$ is the steady creep rate. As shown in Figure 4, the n values of AX61, AT61, and AZ61 samples are given by linearly fitting the plots of steady creep rate with respect to applied stress. The n values of all tested samples are over 5, indicating that the steady creep stage is dominated by dislocation slip instead of grain boundary sliding and solute atom drag effect.^[39,40]

D. Texture Evolution at Creep Duration

Figure 5 shows the typical IPFs and corresponding $\{0001\}$ pole figures of AX61, AT61, and AZ61 samples crept under 80 MPa to 30 hours. Clearly, the three investigated samples show the increased texture intensity with the same intensity order as the initial state, manifesting the inheritance of basal texture after creep loading. Since twinning is sensitive to the tensile loading direction and the present creep direction is adverse for twinning,^[41] only sparse twins are activated. The high Al

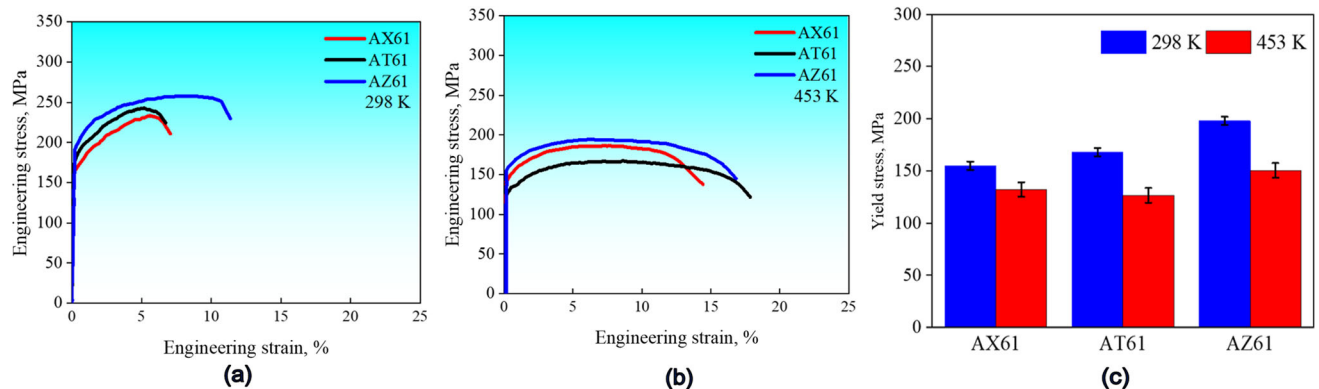


Fig. 2—(a) and (b) Typical engineering stress–strain curves of AX61, AT61, and AZ61 samples along the RD at room temperature and creep temperature; (c) histogram of yield stresses for all the samples.

Table II. Yield Stresses of AX61, AT61, and AZ61 Samples at Room Temperature and Creep Temperature

Sample (K)	AX61 (MPa)	AT61 (MPa)	AZ61 (MPa)
298	155 ± 4	168 ± 4	198 ± 4
453	132 ± 7	127 ± 7	151 ± 7

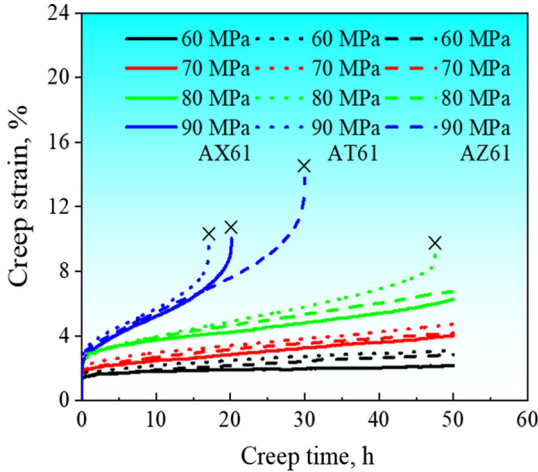


Fig. 3—Tensile creep strain vs. creep time curves of AX61, AT61, and AZ61 samples crept along the RD at 453 K.

Table III. Steady Creep Rate Values of AX61, AT61, and AZ61 Samples Measured Along the RD at 453 K

Applied Stress (σ) (MPa)	Steady Creep Rate ($\dot{\epsilon}$) (s^{-1})		
	AX61	AT61	AZ61
60	9.15×10^{-9}	2.78×10^{-8}	2.14×10^{-8}
70	2.51×10^{-8}	5.06×10^{-8}	3.31×10^{-8}
80	5.26×10^{-8}	1.22×10^{-7}	6.98×10^{-8}
90	1.45×10^{-7}	3.15×10^{-7}	2.44×10^{-7}

contents also make the occurrence of twinning difficult because of solid solution strengthening.^[42] The low twin amounts and the increased texture intensity confirm again that the creep behaviors of these three samples are dominated by dislocation slip. And the addition of Ca, Sn, and Zn elements have a limited effect on the twinning behavior.

E. Dynamic Precipitation at Creep Duration

Figure 6 presents the microstructures of AX61, AT61, and AZ61 samples crept under 80 MPa to 30 hours. The bright and dark contrasts are clearly observed, especially in AZ61 sample. This is caused by the dynamic precipitation at creep duration, which are usually considered to be formed in the vicinity of grain boundaries.^[43] Furthermore, for AZ61 sample, some grains are totally or mainly embraced by the dark contrast, indicating that the fractions of dynamic

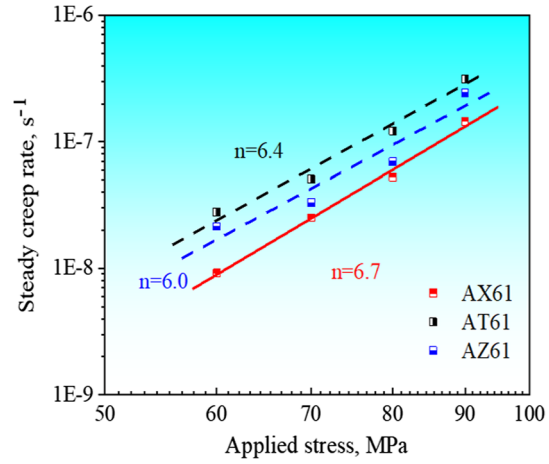


Fig. 4—Ln-Ln plots of steady creep rate vs. applied stress of AX61, AT61, and AZ61 samples crept along the RD at 453 K.

precipitation are obviously higher in comparison to AX61 and AT61 samples.^[8,44] According to the dynamic precipitation behaviors, in the cases of AX61 and AT61 samples, the formation of dynamic precipitation is proposed to be suppressed because of the addition of Ca and Sn elements. Thus, the different fractions of dynamic precipitation related to different adding elements are responsible for the different creep properties.

Using SEM observations, Figure 7 shows the typical precipitate morphologies of AX61, AT61, and AZ61 samples at the creep duration consistent with the OM observations in Figure 6. In both low and high magnifications, there is no doubt that the dynamic precipitates are decorating the grain boundaries and extending from the grain boundaries to the grain interiors, regardless of the adding elements. Using ten pieces or more SEM images and *ImagePro* software, the fractions of dynamic precipitates are manifested to be ~ 7 pct for AX61 sample, ~ 14 pct for AT61 sample, and ~ 31 pct for AZ61 sample. The volume fractions of dynamic precipitates are much higher in AZ61 sample than in AX61 and AT61 samples. In addition, several block-like precipitates are seen in AX61 sample, and some fine precipitates have occupied the grain interiors of AT61 sample. These precipitates may be Ca-containing and Sn-containing phases, but the actual element distributions should be further characterized due to the low contents.

F. Dislocation Mechanism at Creep Duration

Since the rate controlling creep processes in AX61, AT61, and AZ61 samples are dominated by dislocation slip, further observations in dislocation types are performed *via* TEM analysis. Figures 8(a) through (c) exhibit the bright fields for AX61 sample crept under 80 MPa to 30 hours. Due to the fraction of Schmid factor above 0.35 is high in AX61 sample and the critical resolved shear stress (CRSS) for basal slip is low,^[45] it is better to directly observe non-basal dislocations. Under the beam direction $B = [0001]$, dislocation networks can be clearly seen in Figure 8(a). Since all

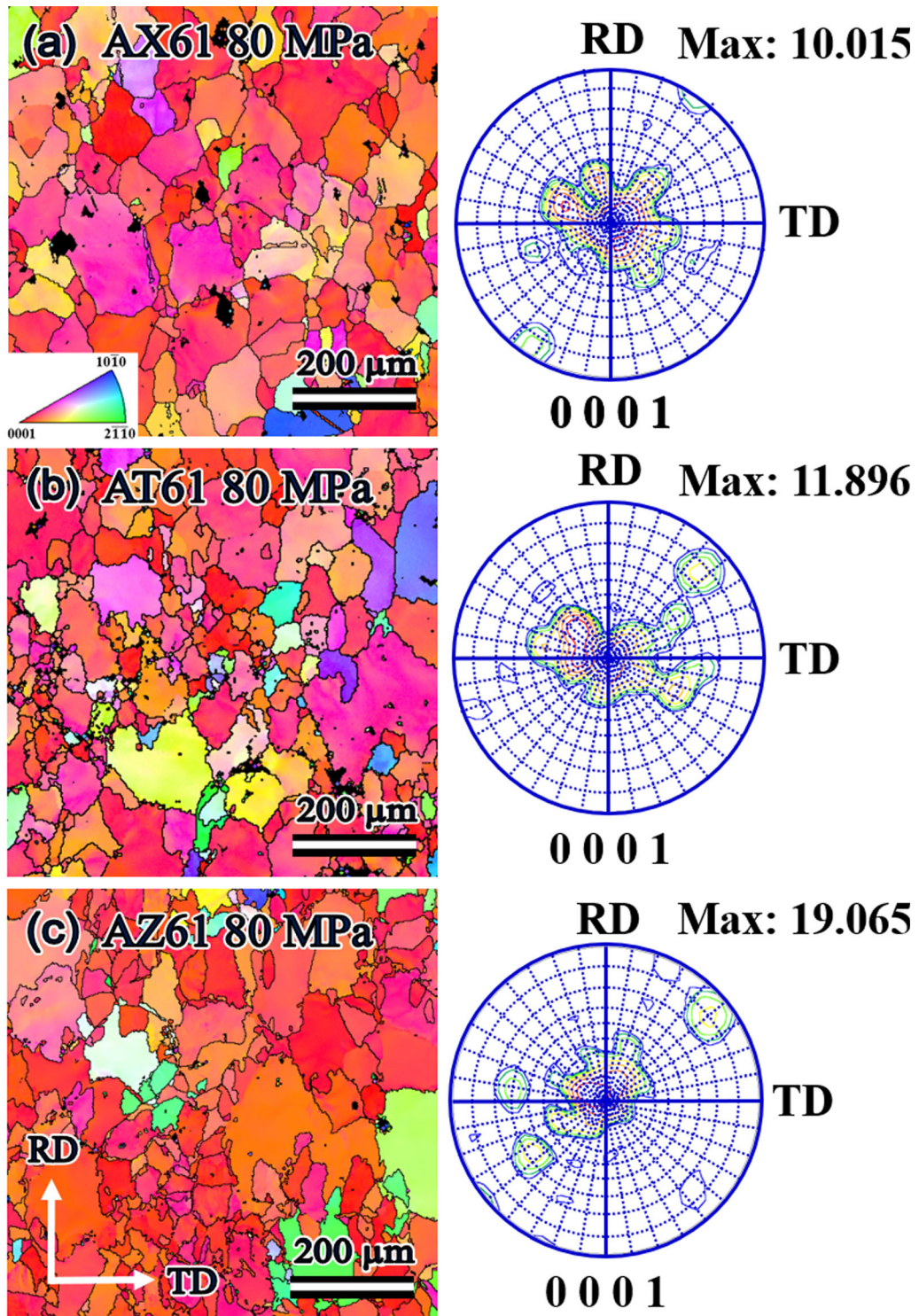


Fig. 5—Typical IPF maps and {0001} pole figures in (a) AX61, (b) AT61, and (c) AZ61 samples crept under 80 MPa to 30 h.

basal $\langle a \rangle$ dislocations have been extinct under $B = [0001]$, the dislocation networks are certainly composed by non-basal dislocations. To make sure the dislocation types, the two-beam mode is performed with two diffraction vectors $g = [10\bar{1}0]$ and $g = [11\bar{2}0]$,

leading to the extinction of all $\langle c \rangle$ components. All $\{10\bar{1}0\}$ prismatic traces are exhibited in the lower right corner, as shown in Figures 8(b) and (c). The observed prismatic dislocations mainly have two slip traces, including the one perpendicular to the $(10\bar{1}0)$ plane

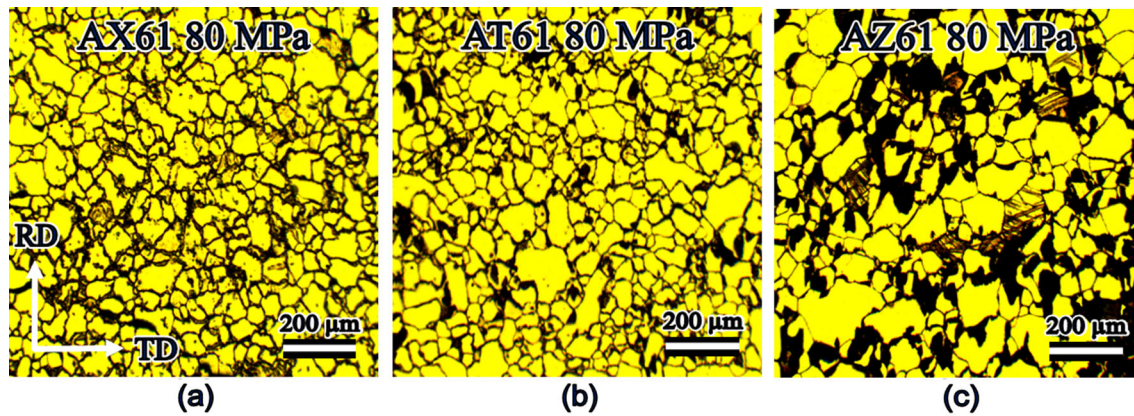


Fig. 6—Typical OM images for (a) AX61, (b) AT61, and (c) AZ61 samples crept under 80 MPa to 30 h.

trace in Figure 8(b) and the other one tilting an angle of 60° to the $(10\bar{1}0)$ plane trace in Figure 8(c). Moreover, the two slip traces are almost parallel to the two main dislocation lines in the networks in Figure 8(a). It is thus indicated that the dislocation networks in AX61 sample are mainly composed by prismatic $\langle a \rangle$ dislocations. Figures 8(d) through (g) exhibit the HAADF image and element mapping results for observing the dynamic precipitates, which are taken under $\mathbf{B} = [0001]$. It is manifested that the block-like precipitates near the grain boundary are only composed by Al element without any Ca element. Namely, the majority of the block-like precipitates observed in the OM and SEM images are the $\text{Mg}_{17}\text{Al}_{12}$ phases, and the low content of Ca element is hard to trigger the fast occurrence of Ca-containing compounds.

Figures 9(a) and (b) present the TEM bright fields for the dislocation configurations in AT61 sample crept under 80 MPa to 30 hours. Due to Sn-containing phase would be much smaller than $\text{Mg}_{17}\text{Al}_{12}$ phase and the habit plane of Sn-containing phase is prismatic plane,^[23,26] the incident beam direction is chosen to be $\mathbf{B} = [\bar{2}110]$. Under the diffraction vector $\mathbf{g} = [01\bar{1}0]$, all $\langle c \rangle$ components are extinct. The remained $\langle a \rangle$ dislocations have long slip traces and large tilt angles to the (0002) plane trace, suggesting that the prismatic $\langle a \rangle$ slip accelerates the creep rate more easily in AT61 sample than in AX61 sample. Here, it should be emphasized that the few observed basal $\langle a \rangle$ dislocations do not mean basal $\langle a \rangle$ slip is rarely activated. Instead, this phenomenon is caused by the covers made by large-scale $\text{Mg}_{17}\text{Al}_{12}$ phases on the basal planes. Under the diffraction vector $\mathbf{g} = [0002]$, all $\langle a \rangle$ components are extinct. The remained dislocations are all consisted of $\langle c \rangle$ components, suggesting that pyramidal $\langle c + a \rangle$ slip is frequently activated in AT61 sample besides prismatic $\langle a \rangle$ slip. Moreover, the occurrence of pyramidal $\langle c + a \rangle$ slip is more frequent in AT61 sample than in AX61 sample. Figures 9(c) through (f) show the HAADF image and element mapping results for observing the dynamic precipitates, which are taken under $\mathbf{B} = [\bar{2}110]$. It is seen that the majority of the dynamic precipitates are $\text{Mg}_{17}\text{Al}_{12}$ phases and some fine

precipitates are consisted of Sn element. Thus, the dynamic precipitation behaviors are different between AX61 and AT61 samples. No Ca is traced in the dynamic precipitates in AX61 sample, while Sn element participates in the dynamic precipitation of AT61 sample.

As a comparison, in Figure 10, TEM bright fields are also performed on AZ61 sample crept under 80 MPa to 30 hours. The incident beam direction is also determined along $\mathbf{B} = [\bar{2}110]$, due to the high-density and large-scale $\text{Mg}_{17}\text{Al}_{12}$ phases will cover the contrast of dislocations under $\mathbf{B} = [0001]$. Two diffraction vectors $\mathbf{g} = [01\bar{1}0]$ and $\mathbf{g} = [0002]$ are selected for the two-beam mode. Then, the $\langle c \rangle$ components and $\langle a \rangle$ components in the dislocations are alternately extinct. It is clearly observed that the frequency of non-basal dislocation slip in AZ61 sample falls in between AX61 and AT61 samples. Specifically, the non-basal dislocations in AZ61 sample are connecting with dynamic precipitates and have no chance to form the dislocation networks like the case in AX61 sample. The slip traces of prismatic $\langle a \rangle$ dislocations and pyramidal $\langle c + a \rangle$ dislocations in AZ61 sample are shorter compared to the slip traces of prismatic $\langle a \rangle$ dislocations in AT61 sample. The shorter slip traces suggest that non-basal dislocations cannot induce the fast increase of creep strain in AZ61 sample as the case in AT61 sample. Additionally, it is no doubt that the dynamic precipitates in AZ61 sample are $\text{Mg}_{17}\text{Al}_{12}$ phases since the dynamic precipitation behavior of AZ series has been widely studied.^[46]

IV. DISCUSSION

A. Similar Grain Boundary Strengthening and Texture Strengthening

In order to discuss the creep resistance, in this work, grain boundary strengthening is firstly estimated by the classical Hall–Petch relationship as a function of grain size^[47]:

$$\sigma_g = kd^{-1/2} \quad [2]$$

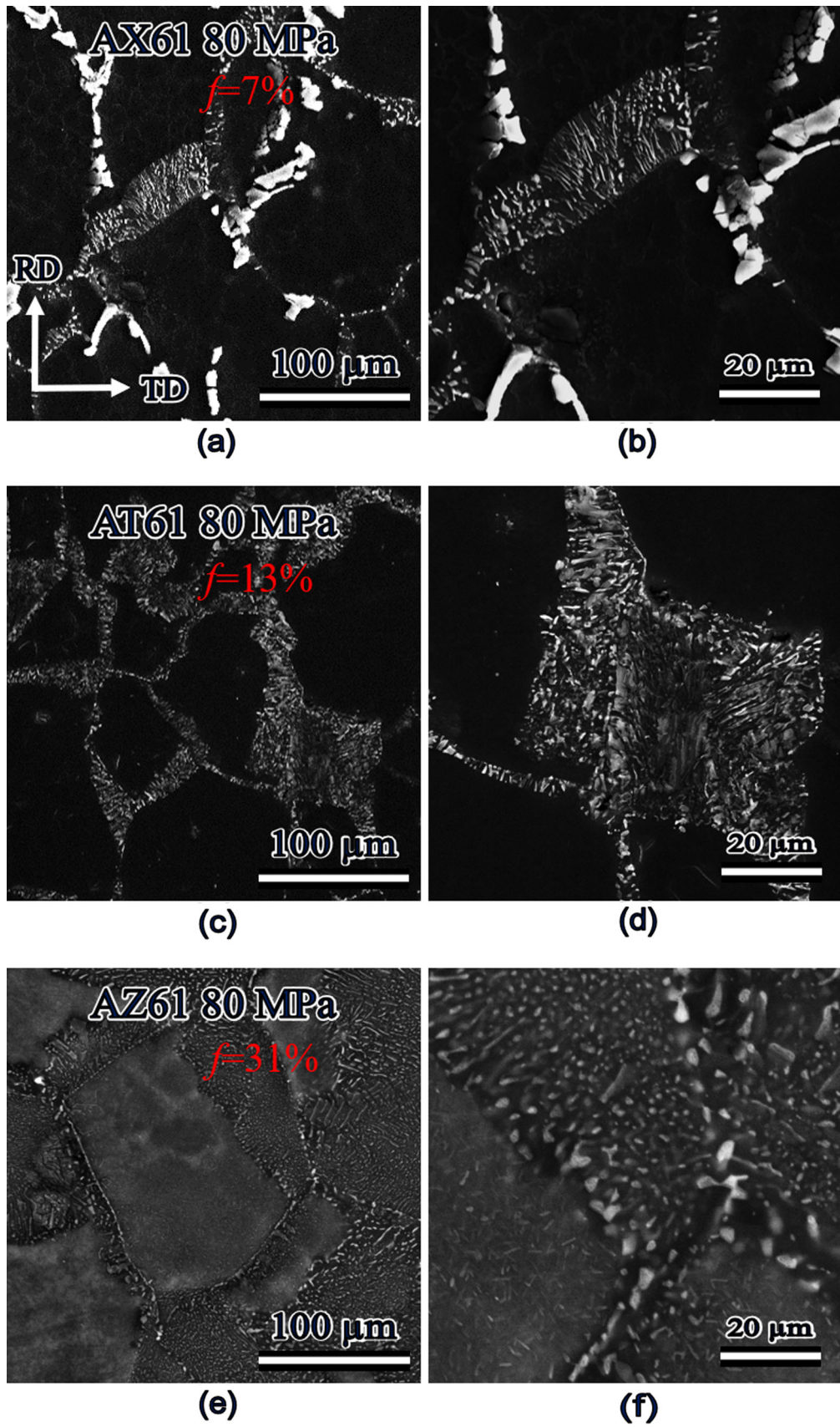


Fig. 7—Typical SEM images showing dynamic precipitates in (a) and (b) AX61 sample, (c) and (d) AT61 sample, and (e) and (f) AZ61 sample crept under 80 MPa to 30 h.

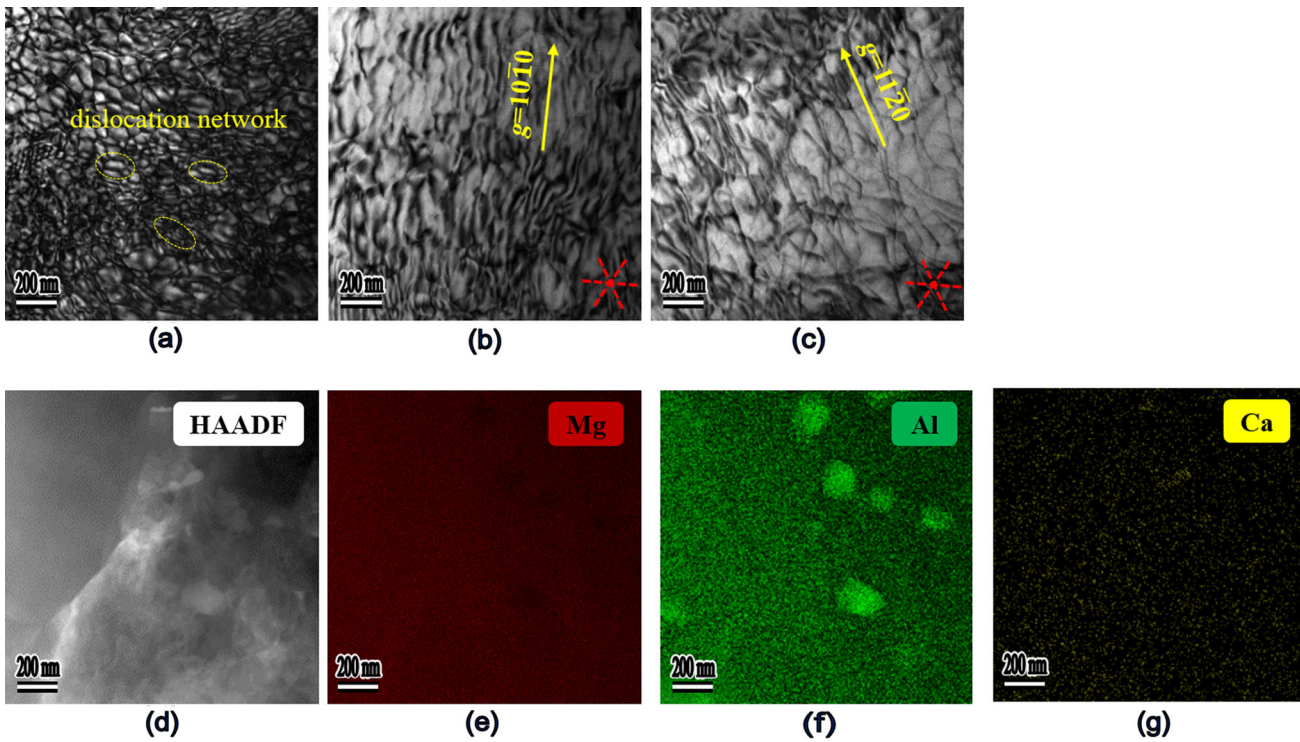


Fig. 8—(a) through (c) TEM bright fields of AX61 sample crept under 80 MPa to 30 h under incident beam direction $\mathbf{B} = [0001]$, and two diffraction vectors (b) $\mathbf{g} = [10\bar{1}0]$ and (c) $\mathbf{g} = [11\bar{2}0]$; (d) HAADF-STEM map and corresponding element distribution maps of (e) Mg element, (f) Al element, and (g) Ca element.

In this equation, σ_g represents the grain boundary strengthening contribution, k denotes the Hall–Petch slope ($281 \text{ MPa} \cdot \mu\text{m}^{1/2}$),^[48] d is the average grain size. From this, the contribution of grain size to the strength can be given in these cases of AX61, AT61, and AZ61 samples. The values are 34 MPa for AX61 sample, 31 MPa for AT61 sample, and 33 MPa for AZ61 sample, respectively. Then, the grain boundary strengthening contribution to the creep resistance of the three samples can be omitted because of the similar values.

Furthermore, the additions of Ca and Sn elements have changed the basal texture intensity, triggering the change of texture strengthening to different samples especially increasing the frequency of basal $\langle a \rangle$ slip. A combination of texture strengthening (σ_t) and grain boundary strengthening (σ_g) can be calculated as^[49]

$$\sigma_t = \sigma_{g+t} - \sigma_g \quad [3]$$

$$\sigma_{g+t} = \sigma_g \frac{0.3}{m} \quad [4]$$

Here, σ_{g+t} denotes the combined contributions of texture strengthening and grain boundary strengthening, and m is the average Schmid factor for basal slip. These m values along the RD of AX61, AT61, and AZ61 samples are 0.25, 0.23, and 0.21 after solid solution, respectively. Therefore, the σ_{g+t} values are 41 MPa for AX61 sample, 42 MPa for AT61 sample, and 47 MPa for AZ61 sample, respectively. Then, the texture strengthening contribution is 7, 10, and 14 MPa

for AX61, AT61, and AZ61 samples. Hence, the texture strengthening contribution to the creep resistance can also be omitted since the differences locate in a narrow stress range.

B. Different Solution Strengthening Contributions

The solution strengthening effect is determined by solute atom and solute concentration. To quantitatively describe this effect, the solution strengthening contribution can be expressed as the equation below^[50–52]:

$$\sigma_s = k_{\text{Al}} \cdot c_{\text{Al}}^n + k_i \cdot c_i^n \quad [5]$$

Here, σ_s is the solution strengthening contribution, k_{Al} and k_i are the strengthening factors of Al element and the third alloying element ($i = \text{Ca, Sn, Zn}$), c_{Al} and c_i are the alloying concentrations of Al element and the third alloying element ($i = \text{Ca, Sn, Zn}$) in atom percent, and n is equal to $2/3$ in Mg alloys. According to the previous studies,^[50,52] the specific values are $k_{\text{Al}} = 196 \text{ MPa} \cdot (\text{at. pct})^{-2/3}$, $k_{\text{Sn}} = 389 \text{ MPa} \cdot (\text{at. pct})^{-2/3}$, and $k_{\text{Zn}} = 905 \text{ MPa} \cdot (\text{at. pct})^{-2/3}$, respectively. Therefore, the solution strengthening contribution is 34.7 MPa for AT61 sample and 47.6 MPa for AZ61 sample. The k_{Ca} value cannot be directly obtained in the published reports. However, in the work done by Abaspour *et al.*,^[51] the solution strengthening effect brought by Ca was found to be comparable to the solution strengthening effect brought by Gd, Nd, and Y. Since the related data and fitted line of Ca are located between

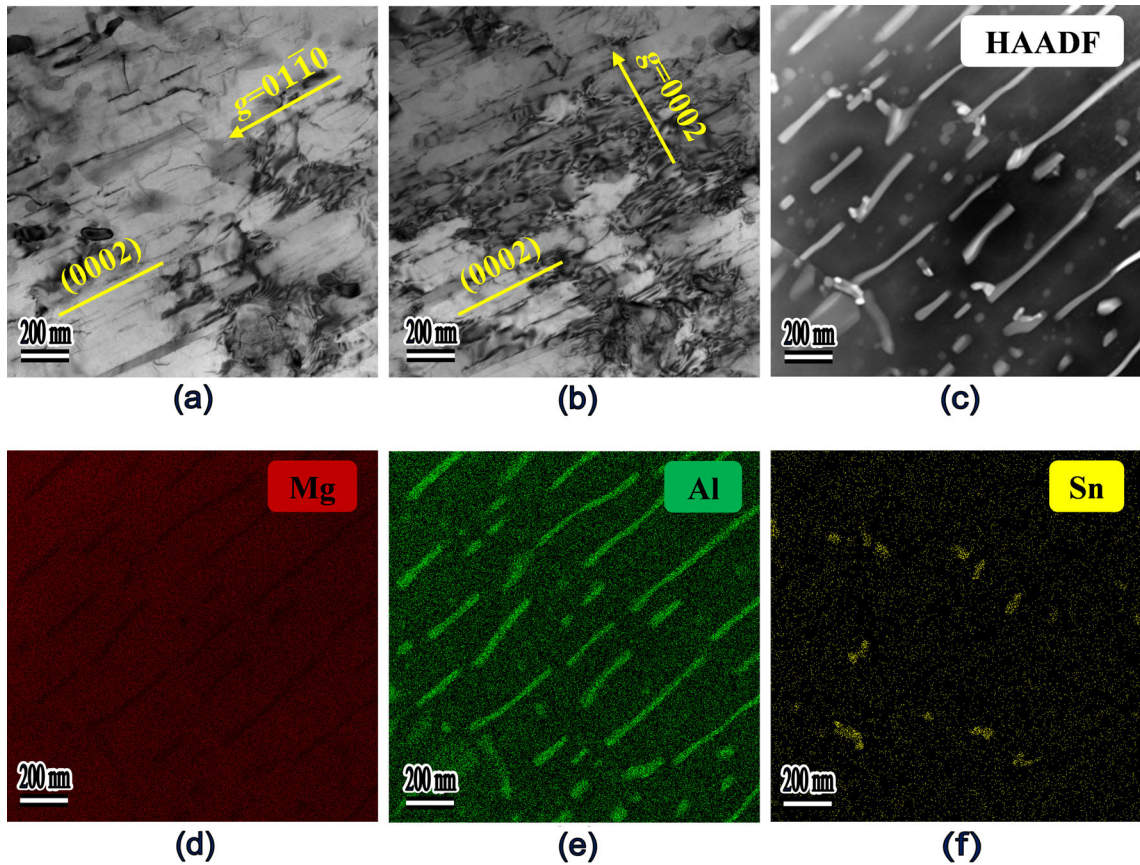


Fig. 9—(a) and (b) TEM bright fields of AT61 sample crept under 80 MPa to 30 h under incident beam direction $\mathbf{B} = [2\bar{1}10]$, and two diffraction vectors (a) $\mathbf{g} = [01\bar{1}0]$ and (b) $\mathbf{g} = [0002]$; (c) HAADF-STEM map and corresponding element distribution maps of (d) Mg element, (e) Al element, and (f) Sn element.

the data and fitted lines of Gd and Y in their work, the k_{Ca} value should be 1168 to 1249 MPa·(at. pct) $^{-2/3}$. Then, the solution strengthening contribution is 65.5 to 67.6 MPa for AX61 sample. It is clearly seen that adding Ca provides the strongest solution strengthening. Moreover, Ca element does not participate in dynamic precipitation as shown in Figure 8, resulting in the lowest loss of solution strengthening during creep loading.

C. Different Precipitation Strengthening Contributions

From the results in Figures 7 through 10, it is known that both $Mg_{17}Al_{12}$ and Mg_2Sn phases exist in AT61 sample, while only $Mg_{17}Al_{12}$ phases exist in AX61 and AZ61 samples. If all the precipitates provide effective precipitation strengthening during creep loading, the precipitation strengthening contribution (σ_p) can be written as^[7]

$$\sigma_p = \frac{Gb}{2\pi\sqrt{1-\nu}\left(\frac{0.953}{\sqrt{f}} - 1\right)d_t} \ln \frac{d_t}{b} \quad [6]$$

In this equation, G represents the shear modulus of Mg matrix (1.66×10^4 MPa), b is the Burgers vector

length of basal $\langle a \rangle$ dislocation (0.32 nm), ν is the Poisson's ratio (0.35), f is the precipitate fraction, and d is the average precipitate diameter. According to Eq. [6], the assumed precipitation strengthening contribution in AX61, AT61, and AZ61 samples is 26, 35, and 95 MPa, respectively. For AX61 sample, the low $Mg_{17}Al_{12}$ fraction consumes only a slight degree of solution strengthening. For AT61 sample, although some reports have indicated that $Mg_{17}Al_{12}$ and Mg_2Sn phases are frequently symbiotic,^[44,53] the Mg_2Sn fraction is only 0.83 pct due to the low Sn addition in this work. Consequently, not only the formation of $Mg_{17}Al_{12}$ phases is slower in AT61 sample compared to AZ61 sample, but also the low fraction of Mg_2Sn phases hardly contributes to the precipitation strengthening. The consumption of solution strengthening fails in obtaining excellent precipitation strengthening.

On the other hand, it should be noted that the distributions of dynamic precipitates in the three samples are different. In AX61 sample, almost all dynamic precipitates are distributed at the grain boundaries. In contrast, in AT61 and AZ61 samples, dynamic precipitates are distributed in the grain interiors besides the grain boundaries. According to the transitivity of dislocation slip across grain boundary,^[54,55] the dynamic precipitates at grain boundaries can interrupt the successive slip transition from one grain to its adjacent

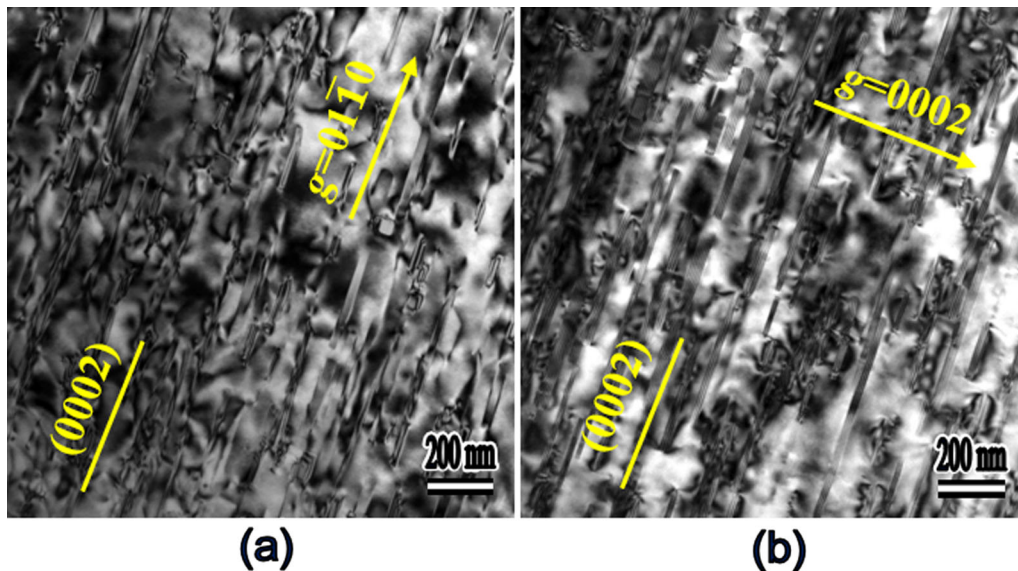


Fig. 10—(a) and (b) TEM bright fields of AZ61 sample crept under 80 MPa to 30 h under incident beam direction $B = [2\bar{1}10]$, and two diffraction vectors (a) $g = [0\ 1\bar{1}0]$ and (b) $g = [0002]$.

grain and finally slow down the creep rate. Using the MATLAB Software with MTEX 5.8.1 toolbox and the EBSD data of solution-treated samples in Figure 1, Figure 11 presents the transitivity maps for different slip systems across grain boundaries. The coordinate on the right side corresponds to the transitivity ability. For example, yellow grain boundary has better transitivity ability than blue grain boundary. One slip system easily persists in the neighboring grain after transferring the yellow grain boundary; otherwise, the slip system is interrupted at the blue grain boundary and fails in penetrating into the neighboring grain. In Figure 11, it is seen that the slip transitivity for basal slip shows quite different results while the slip transitivity for non-basal slip shows similar color distributions among the three samples. The widespread distribution of yellow grain boundaries suggests that basal slip would be the most active in AX61 sample if no precipitates exist at the grain boundaries. This is the reason for the lower yield stress of AX61 sample compared to AZ61 sample, which is also consistent with the high fraction of Schmid factor above 0.35 in Figure 1. During creep loading, dynamic precipitates are gradually formed at the grain boundaries of AX61 sample. The transitivity ability for basal slip in AX61 sample is thus continuously weakened, which is beneficial for the improvement of creep resistance. But for AZ61 sample, the Schmid factors above 0.35 have a lower fraction compared to AX61 sample. So the precipitates at the grain boundaries have an inconspicuous effect on the basal slip transitivity of AZ61 sample, and limitedly contribute to the improvement of creep resistance.

D. Different Dislocation Morphologies

Apart from the above-mentioned interactions between precipitates and dislocations, the dislocation morphology is also responsible for the creep resistance. In AX61 sample, dislocation networks composed by prismatic $\langle a \rangle$ dislocations are found. According to the previous reports,^[56–58] dislocation networks have been confirmed as the stable and non-deformable microstructure for Mg alloys. Hence, such dislocation morphology can effectively delay the increase of creep strain. On the contrary, in AT61 sample, prismatic $\langle a \rangle$ dislocations leave long slip traces, suggesting that the creep rate is prominently improved. And the frequent pyramidal $\langle c + a \rangle$ slip further triggers the increase of creep strain since pyramidal $\langle c + a \rangle$ slip always promotes the easy plastic deformation.^[59] Wang *et al.*^[60] have investigated the effects of Al and Sn on the stacking fault energy in order to predict the pyramidal $\langle c + a \rangle$ slip activity in Mg alloys. Their results showed that Sn element contributed more to the reduction of stacking fault energy than Al element, which is consistent with the frequent pyramidal $\langle c + a \rangle$ slip in AT61 sample of our present work. In AZ61 sample, the close connection between precipitates and non-basal dislocations avoids the fast increase of creep strain induced by long slip traces like the case in AT61 sample.

As a summary, for AX61 alloy, adding Ca element provides outstanding solution strengthening. During creep loading, the dynamic precipitation slightly consumes solution strengthening, and the precipitates at the grain boundaries effectively interrupt the basal slip transition between neighboring grains. The dislocation

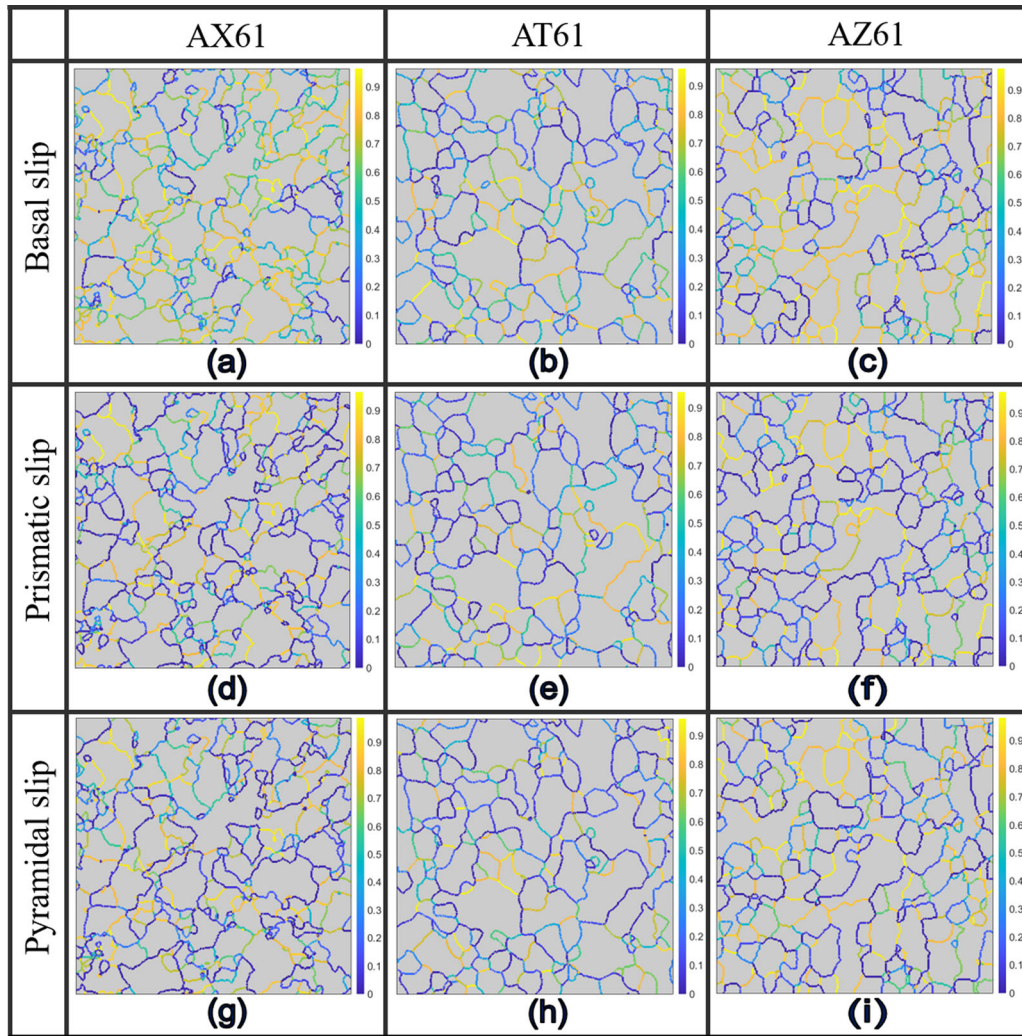


Fig. 11—Slip transitivity maps of AX61, AT61, and AZ61 samples for (a) through (c) basal slip, (d) through (f) prismatic slip, and (g) through (i) secondary pyramidal slip across grain boundaries after solid solution treatments.

networks made by prismatic $\langle a \rangle$ dislocations further enhance the creep resistance. For AT61 alloy, the solution strengthening is consumed but the precipitation strengthening is not strong enough for enhancing the creep resistance. The long slip traces of prismatic $\langle a \rangle$ dislocations further increase the creep rate. For AZ61 alloy, strong precipitation strengthening is obtained from the large consumption of solution strengthening. Although the precipitation strengthening can avoid the weakened creep resistance like the case in AT61 alloy, it is still insufficient to enhance the creep resistance as strong as that of AX61 alloy. In addition, the effects of grain size, texture intensity, and twinning on the creep resistance are close among the three alloys.

V. CONCLUSIONS

In this study, taking AZ61 alloy into account as a suitable comparison, a comprehensive investigation on the effects of different alloying elements (Ca, Sn, and

Zn) on the creep resistance of Mg–Al-based alloys is carried out at 453 K. The main conclusions are summarized as follows:

1. Under uniaxial tensile loading, AZ61 alloy has the highest yield stress due to the slightly higher basal texture intensity. However, AX61 alloy owns the strongest creep resistance under tensile creep loading, followed by AZ61 alloy, and the weakest creep resistance is found in AT61 alloy.
2. Adding Ca element provides the most effective solution strengthening for the creep resistance. During creep loading, no Ca-containing precipitates are formed, resulting in the lowest loss of solution strengthening for the creep resistance of AX61 alloy. Inversely, Sn element is detected in the dynamic precipitates of AT61 alloy and the highest $\text{Mg}_{17}\text{Al}_{12}$ fraction is obtained in AZ61 alloy, inducing the obviously reduced solution strengthening for the creep resistance.
3. The basal slip transitivity between neighboring grains is reduced the most effectively in AX61

alloy, which further enhances the creep resistance. However, for AT61 alloy, the consumption of solution strengthening fails in achieving sufficient precipitation strengthening. For AZ61 alloy, the dramatic precipitation strengthening avoids the sharply weakened creep resistance like the case in AT61 alloy.

- Dislocation slip controls the creep processes of all three alloys. Dislocation networks made by prismatic $\langle a \rangle$ dislocations strongly enhance the creep resistance of AX61 alloy. Long slip traces induced by prismatic $\langle a \rangle$ dislocations and profuse pyramidal $\langle c + a \rangle$ slip accelerate the creep rate of AT61 alloy. For AZ61 alloy, non-basal dislocations closely connect with dynamic precipitates, leading to the shorter slip trace and stronger creep resistance compared to AT61 alloy.

ACKNOWLEDGMENTS

The authors gratefully acknowledge the financial supports received from the National Natural Science Foundation of China (Grant Nos. 51974376 and 52071344), the Natural Science Foundation of Hunan Province (Grant No. 2021JJ20063), and the Distinguished Professor Project of Central South University (Grant No. 202045009).

CONFLICT OF INTEREST

The authors declare that they have no conflict of interest.

REFERENCES

- Q. Huo, X. Yang, J. Ma, H. Sun, J. Qin, and Y. Jiang: *Mater. Charact.*, 2013, vol. 29, pp. 43–51.
- J.U. Lee, Y.J. Kim, and S.H. Park: *Mater. Sci. Eng. A*, 2022, vol. 854, p. 143814.
- A. Jamali, A. Ma, and J. LLorca: *Acta Mater.*, 2022, vol. 239, p. 118263.
- T. Chen, S. Hu, S. Li, and Q. Huo: *Mater. Sci. Eng. A*, 2022, vol. 857, p. 144056.
- P. Nautiyal, J. Jain, and A. Agarwal: *Mater. Sci. Eng. A*, 2015, vol. 630, pp. 131–38.
- S. Spigarelli: *Scripta Mater.*, 2000, vol. 42, pp. 397–402.
- J.F. Nie: *Scripta Mater.*, 2003, vol. 48, pp. 1009–15.
- B. Amir Esgandari, H. Mehrjoo, B. Nami, and S.M. Miresmaeili: *Mater. Sci. Eng. A*, 2011, vol. 528, pp. 5018–24.
- S.M. Ashrafizadeh, R. Mahmudi, and A.R. Geranmayeh: *Mater. Sci. Eng. A*, 2020, vol. 790, p. 139712.
- N. Kashefi and R. Mahmudi: *Mater. Des.*, 2012, vol. 39, pp. 200–10.
- A.R. Geranmayeh and R. Mahmudi: *Mater. Sci. Eng. A*, 2014, vol. 614, pp. 311–18.
- J. Majhi and A.K. Mondal: *Mater. Sci. Eng. A*, 2019, vol. 744, pp. 691–703.
- C.R. Hutchinson, J.F. Nie, and S. Gorsse: *Metall. Mater. Trans. A*, 2005, vol. 36A, pp. 2093–2105.
- P. Hidalgo-Manrique and J.D. Robson: *Metall. Mater. Trans. A*, 2019, vol. 50A, pp. 3855–67.
- S.M. Ashrafizadeh and R. Mahmudi: *Metall. Mater. Trans. A*, 2019, vol. 50A, pp. 5957–68.
- F. Khomamizadeh, B. Nami, and S. Khoshkhouei: *Metall. Mater. Trans. A*, 2005, vol. 36A, pp. 3489–94.
- F. Kabirian and R. Mahmudi: *Metall. Mater. Trans. A*, 2010, vol. 41A, pp. 3488–98.
- T. Nakata, C. Xu, R. Ajima, K. Shimizu, S. Hanaki, T.T. Sasaki, L. Ma, K. Hono, and S. Kamado: *Acta Mater.*, 2017, vol. 130, pp. 261–70.
- M.R. Sahu, T.S.S. Kumar, and U. Chakkingal: *J. Magnesium Alloys*, 2022, vol. 10, pp. 2094–2117.
- S. Li, Q. Huo, S. Hu, C. Wang, Z. Zhang, Y. Zhang, T. Chen, and X. Yang: *Mater. Charact.*, 2023, vol. 195, p. 112534.
- J. Li, X. Zhou, J. Su, B. Breitbach, M.L. Chwałek, H. Wang, and G. Dehm: *Mater. Sci. Eng. A*, 2022, vol. 856, p. 143898.
- T.T. Sasaki, K. Oh-ishi, T. Ohkubo, and K. Hono: *Scripta Mater.*, 2006, vol. 55, pp. 251–54.
- T.T. Sasaki, K. Oh-ishi, T. Ohkubo, and K. Hono: *Mater. Sci. Eng. A*, 2011, vol. 530, pp. 1–8.
- R.E. Schäublin, M. Becker, M. Cihova, S.S.A. Gerstl, D. Deiana, C. Hébert, S. Pogatscher, P.J. Uggowitzer, and J.F. Löffler: *Acta Mater.*, 2022, vol. 239, p. 118223.
- B. Kondori and R. Mahmudi: *Mater. Sci. Eng. A*, 2017, vol. 700, pp. 438–47.
- M.A. Gibson, X. Fang, C.J. Bettles, and C.R. Hutchinson: *Scripta Mater.*, 2010, vol. 63, pp. 899–902.
- D.H. Kang, S.S. Park, and N.J. Kim: *Mater. Sci. Eng. A*, 2005, vol. 413–414, pp. 555–60.
- J. Miao, C. Zhang, A.D. Klarner, J. Zhang, E. Cinkilic, F. Zhang, and A.A. Luo: *Materialia*, 2022, vol. 21, p. 101348.
- J. Li, X. Zhou, A. Breen, Z. Peng, J. Su, P. Kürstner, M.J.D. Correa, M.L. Chwałek, H. Wang, D. Holec, J. Mayer, and G. Dehm: *J. Alloys Compd.*, 2022, vol. 928, p. 167177.
- A.A. Luo, P. Fu, L. Peng, X. Kang, Z. Li, and T. Zhu: *Metall. Mater. Trans. A*, 2012, vol. 43A, pp. 360–68.
- A.S.H. Kabir, M. Sanjari, J. Su, I. Jung, and S. Yue: *J. Mater. Sci.*, 2016, vol. 51, pp. 1600–09.
- S.M. Zhu, B.L. Mordike, and J.F. Nie: *Mater. Sci. Eng. A*, 2008, vol. 483–484, pp. 583–86.
- B.H. Kim, K.C. Park, Y.H. Park, and I.M. Park: *Mater. Sci. Eng. A*, 2011, vol. 528, pp. 808–14.
- A. Bahmani, S. Arthanari, and K.S. Shin: *J. Magnesium Alloys*, 2019, vol. 7, pp. 38–46.
- S. Avraham, A. Katsman, and M. Bamberger: *J. Mater. Sci.*, 2011, vol. 46, pp. 6941–51.
- T. Nakata, C. Xu, Y. Uehara, T.T. Sasaki, and S. Kamado: *J. Alloys Compd.*, 2019, vol. 782, pp. 304–14.
- X. Huang, K. Suzuki, Y. Chino, and M. Mabuchi: *J. Alloys Compd.*, 2015, vol. 632, pp. 94–102.
- Y. Zhang, T. Chen, J. Kuang, and Q. Huo: *Metall. Mater. Trans. A*, 2022, vol. 3A, pp. 747–53.
- C. Wang, Y. Zhang, Q. Huo, Z. Zhang, J. Tang, A. Hashimoto, and X. Yang: *Mater. Sci. Eng. A*, 2021, vol. 800, p. 140309.
- S. Hu, Q. Huo, C. Wang, Y. Zhang, Z. Zhang, S. Xu, and X. Yang: *J. Alloys Compd.*, 2022, vol. 895, p. 162666.
- Y. Zhang, Q. Huo, Z. Zhang, C. Wang, H. Nagami, and X. Yang: *Mater. Sci. Eng. A*, 2022, vol. 839, p. 142894.
- D. Nagarajan: *Mater. Sci. Eng. A*, 2022, vol. 860, p. 144292.
- B. Kim, B. Kang, Y. Park, and I. Park: *Mater. Sci. Eng. A*, 2011, vol. 528, pp. 5747–53.
- S.M. Jo, S.D. Kim, T. Kim, Y. Go, C. Yang, B.S. You, and Y.M. Kim: *J. Alloys Compd.*, 2018, vol. 749, pp. 794–802.
- N. Li, C. Wang, M.A. Monclús, L. Yang, and J.M. Molina-Aldareguia: *Acta Mater.*, 2021, vol. 221, p. 117374.
- H.S. Kim and W.J. Kim: *Corros. Sci.*, 2013, vol. 75, pp. 228–38.
- M.R. Barnett, Z. Keshavarz, A.G. Beer, and D. Atwell: *Acta Mater.*, 2004, vol. 52, pp. 5093–5103.
- A. Jain, O. Duygulu, D.W. Brown, C.N. Tomé, and S.R. Agnew: *Mater. Sci. Eng. A*, 2008, vol. 486, pp. 545–55.
- G. Li, J. Zhang, R. Wu, S. Liu, B. Song, Y. Jiao, Q. Yang, and L. Hou: *J. Alloys Compd.*, 2019, vol. 777, pp. 1375–85.
- L. Gao, R.S. Chen, and E.H. Han: *J. Alloys Compd.*, 2009, vol. 481, pp. 379–84.
- S. Abaspour, V. Zambelli, M. Dargusch, and C.H. Cáceres: *Mater. Sci. Eng. A*, 2016, vol. 673, pp. 114–21.

52. B.Q. Shi, R.S. Chen, and W. Ke: *J. Alloys Compd.*, 2011, vol. 509, pp. 3357–62.
53. J. Miao, W. Sun, A.D. Klarner, and A.A. Luo: *Scripta Mater.*, 2018, vol. 154, pp. 192–96.
54. M. Sarebanzadeh, A. Orozco-Caballero, and J. LLorca: *Acta Mater.*, 2023, vol. 243, p. 118536.
55. C.M. Cepeda-Jiménez, J.M. Molina-Aldareguia, and M.T. Pérez-Prado: *Acta Mater.*, 2015, vol. 88, pp. 232–44.
56. Z. Zhang, Q. Huo, Z. Xiao, Y. Zhang, K. Li, H. Nagaumi, and X. Yang: *J. Mater. Sci.*, 2022, vol. 57, pp. 2229–42.
57. J. Li, J. Wu, L. Jin, M. Celikin, F. Wang, S. Dong, and J. Dong: *Sci. Rep.*, 2021, vol. 11, p. 2860.
58. Y. Liu, J. Yan, D. Xie, Y. Shen, J. Wang, and G. Zhu: *Scripta Mater.*, 2021, vol. 191, pp. 86–89.
59. D. Zhao, X. Ma, S. Picak, I. Karaman, and K. Xie: *Scripta Mater.*, 2020, vol. 179, pp. 49–54.
60. C. Wang, H. Zhang, H. Wang, G. Liu, and Q. Jiang: *Scripta Mater.*, 2013, vol. 69, pp. 445–48.

Publisher's Note Springer Nature remains neutral with regard to jurisdictional claims in published maps and institutional affiliations.

Springer Nature or its licensor (e.g. a society or other partner) holds exclusive rights to this article under a publishing agreement with the author(s) or other rightsholder(s); author self-archiving of the accepted manuscript version of this article is solely governed by the terms of such publishing agreement and applicable law.